

Article

Influence of Properties of Hydraulic Fluid on Pressure Peaks in Axial Piston Pumps' Chambers

Piotr Patrosz 

Faculty of Mechanical Engineering and Ship Technology, Gdansk University of Technology,
ul. Gabriela Narutowicza 11/12, 80-233 Gdańsk, Poland; piotr.patrosz@pg.edu.pl; Tel.: +48-583472831

Abstract: The article concentrates on the research of the pressure peaks in a working chamber of an axial piston pump. The main focus of the article is the influence of fluid properties on the pressure peaks value. Experimental and analytical methods were used to determine the impact of the fluid density, viscosity, compressibility and aeration. The article describes the pressure peak generation process and explains the theoretical basis of this phenomenon. A model of aerated fluid compression and models of leakage were created using CFD analysis and mathematical equations. These partial models were then merged into one consistent model in Matlab Simulink. The final result was verified by comparing the results obtained from the mathematical model with the results of the experiment. After validation, the model was used to present explicitly how each of the mentioned fluid properties affects the pressure peak value. Additionally, the test stand and measurement equipment used in the experiment were presented along with a short description of the laboratory research and sample results.

Keywords: hydraulics; axial piston pumps; pressure peak; fluid properties; compressibility



Citation: Patrosz, P. Influence of Properties of Hydraulic Fluid on Pressure Peaks in Axial Piston Pumps' Chambers. *Energies* **2021**, *14*, 3764. <https://doi.org/10.3390/en14133764>

Academic Editor: Pasquale G. F. Filianoti

Received: 17 May 2021
Accepted: 18 June 2021
Published: 23 June 2021

Publisher's Note: MDPI stays neutral with regard to jurisdictional claims in published maps and institutional affiliations.



Copyright: © 2021 by the author. Licensee MDPI, Basel, Switzerland. This article is an open access article distributed under the terms and conditions of the Creative Commons Attribution (CC BY) license (<https://creativecommons.org/licenses/by/4.0/>).

1. Introduction

Axial piston pumps are the core of modern hydraulic drives, widely described in the literature [1–3]. They are used to supply fluid at high pressures to either complex hydraulic systems, such as the ones mentioned in [4,5], or simpler hydraulic equipment described in [6,7]. Every axial piston pump (Figure 1) consists of a cylinder block (4), moving pistons (3) and is pushed by the swashplate (6). The space created between the piston and the cylinder block is called the working chamber but further in the article it will just be called “the chamber”. Moving pistons suck the fluid into the chamber when they are moving outwards and pump the fluid out of the chamber when moving inwards. In a typical axial piston pump, the commutation plate (7) is used to switch the connection of the chambers between high- and low-pressure channels to ensure the right direction of fluid flow. A change in the connected channels occurs when the volume of the chamber is minimal or maximal. These are the situations when the velocity of the pistons is minimal. Therefore, when the chamber is briefly cut off from both high- and low-pressure channels, the pressure in the chamber does not rise excessively; however, it still causes noise and vibration.

The simplest solution to the problem is not to permit fully cutting off the chamber or to increase the “dead volume” of the chamber. Such solutions are presented in articles focusing on flow ripple reduction [8–10], which is an undesired indirect result of pressure peaks. These solutions have their disadvantages; for example, they decrease the volumetric efficiency of the pump. Therefore, it is very important to research and analyze the pressure peak problem in order to find alternative methods to compensate for it.

Pressure peaks have a much bigger impact on the prototype axial piston pump invented at Gdansk University of Technology by Osiecki and Osiecki [11], because it has a different type of commutation unit. The invented pump is called PWK, which stands for an axial piston pump with a cam-driven commutation unit in Polish. The construction of

the pump is shown in Figure 2. The work principle of the PWK pump is similar to any other axial piston pump. The pistons (4) are pushed by the swashplates (7). The main difference between the typical axial piston pump and PWK pump is the dual construction. This type of construction demands a different type of commutation unit. In this case, it consists of a commutation tube (9) that switches the connection of the working chamber, marked in yellow, between the high-pressure (red) and low-pressure (blue) channel. The commutation tubes are pushed by the cam (11), which rotates with the shaft (1).

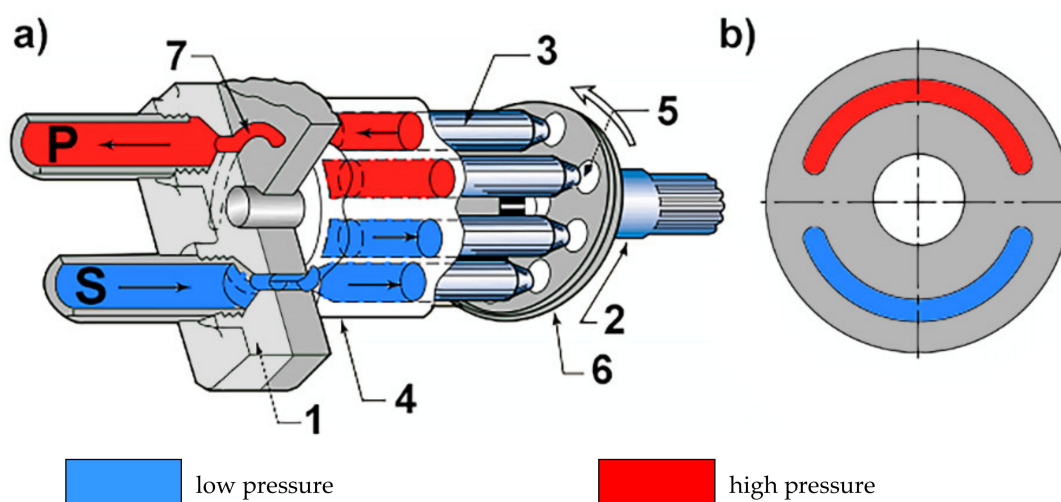


Figure 1. Axial piston pump with plate commutation unit [12]: (a) cross-section of the pump; (b) commutation plate; P—high-pressure pumping channel; S—low-pressure suction channel; 1—manifold; 2—shaft; 3—piston; 4—cylinder block; 5—slipper; 6—swashplate; 7—commutation plate.

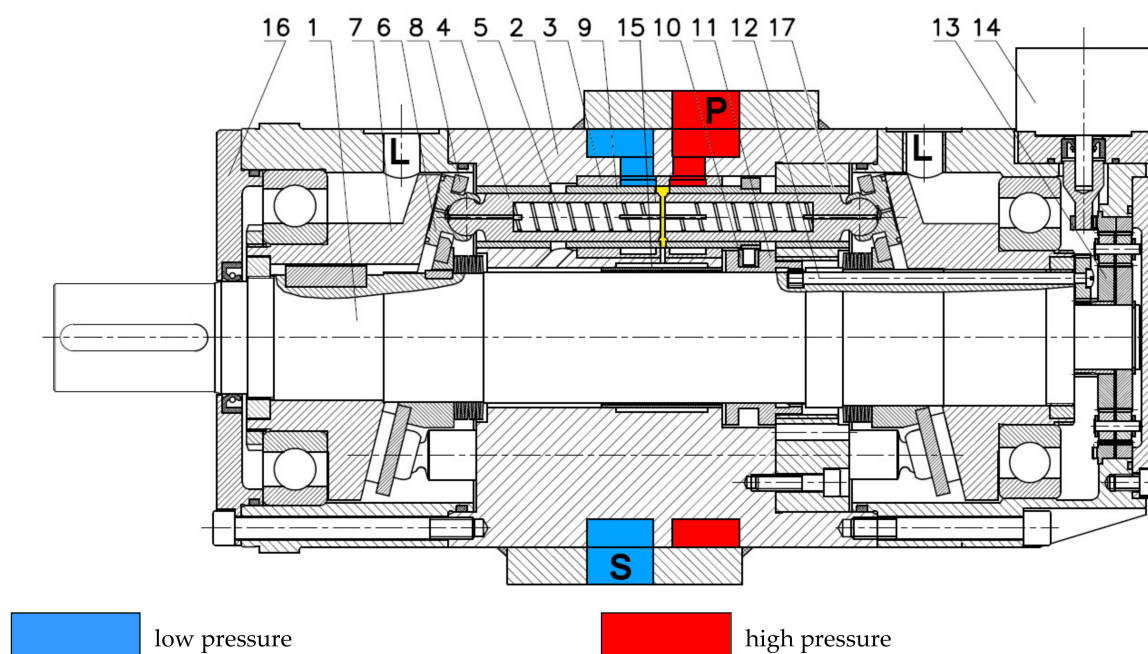


Figure 2. Axial piston pump with cam-driven commutation unit (PWK) [12]: P—high-pressure pumping channel; S—low-pressure suction channel; L—leakage channel; 1—shaft; 2—body; 3—socket; 4—piston; 5—spiral choke; 6—slipper; 7—swash-plate; 8—separator plate; 9—commutation tube; 10—cam slipper; 11—cam; 12—adjustment shaft; 13—gearbox; 14—adjustment motor; 15—compensation tube; 16—cover; 17—guiding tube.

One cycle of the PWK pump's working chamber volume change at 100% displacement is presented in Figure 3.

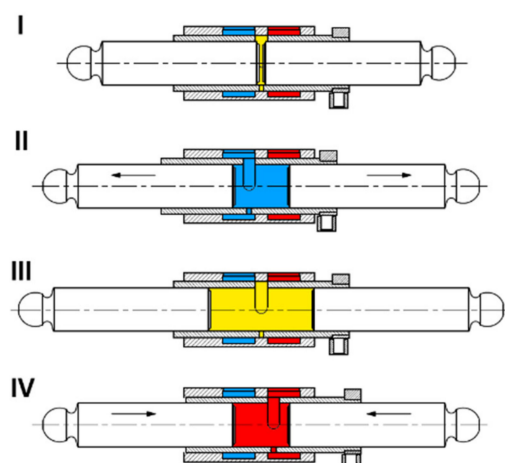


Figure 3. Cycle of the PWK pump's working chamber volume change at 100% displacement [12].

Phase I is the beginning of the process when the chamber is disconnected from the high/low-pressure channels, and the pistons' velocity is near zero. Phase II presents the suction phase when the chamber is connected to the low-pressure channel and the pistons are moving apart. Phase III is the switching phase when the chamber is cut-off and the piston velocity is near zero. Phase IV is the pumping phase when the pistons are getting closer.

Typically, to alter the displacement of an axial piston pump, it is necessary to change the angle of the swashplate. This process and associated problems are described in articles [13,14]. Pumps with a cam-driven commutation unit have a different way of adjusting the displacement. If the cam is rotated separately from the shaft, it changes the moment at which the connection between the chamber and high/low-pressure channels are switched. One cycle of the PWK pump's working chamber volume change at decreased displacement is presented in Figure 4.

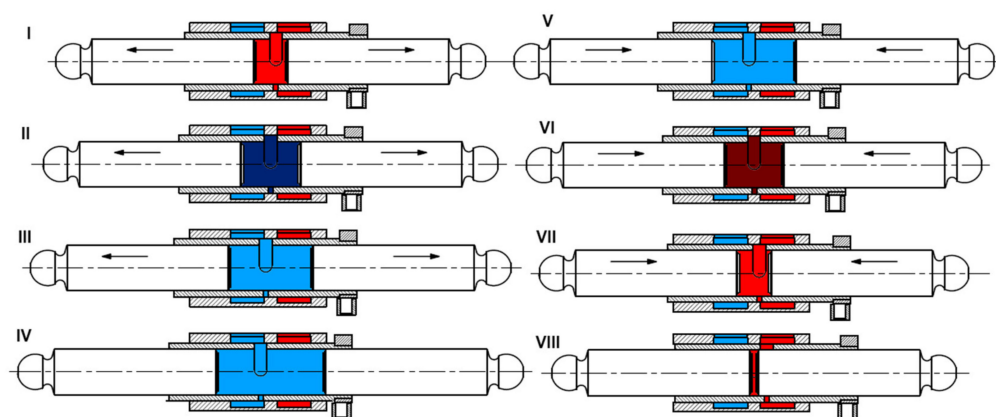


Figure 4. Cycle of the PWK pump's working chamber volume change at decreased displacement [12].

Phase I shows the beginning of the suction process when the fluid is sucked from the high-pressure channel. Phase II presents the switching process when the chamber is cut-off and the pistons are moving apart. In this phase, cavitation may occur. Phase III is the continuation of the suction process when the fluid is sucked from the low-pressure channel. The longer Phase III lasts, in comparison with Phase I, the higher will be the displacement of the pump. Phase IV indicates the moment when the pistons change the direction of their movement. Phase V is the beginning of the pumping process when the pistons are getting closer to each other and the chamber is connected to the low-pressure channel. Phase VI is the moment when high-pressure peaks occur, because the moving pistons still generate a sudden pressure rise in the cut-off chamber. This phase will be the focus of this article

and all calculations included in this paper will concern it. Phases VII and VIII show the continuation of the pumping process when the fluid is pumped from the chamber into the high-pressure channel.

The pressure peak p_p is defined as the difference between the maximal measured pressure inside the chamber p_{max} and the pumping pressure p_o , which is described by Equation (1) and presented in Figure 5.

$$p_p = p_{max} - p_o \quad (1)$$

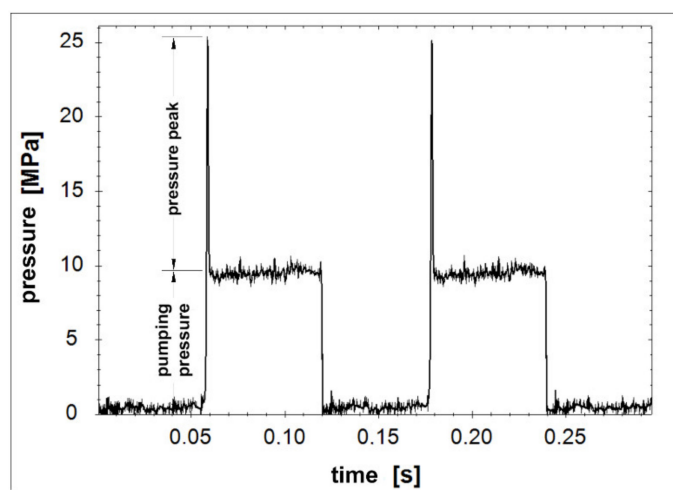


Figure 5. Sample characteristics of the pressure changes inside the working chamber and pressure peak definition [12].

The pressure peaks are influenced by many factors, which change their values directly or indirectly by affecting the other factors. A graph presenting the grid of connections between the factors and pressure peaks phenomenon is shown in Figure 6.

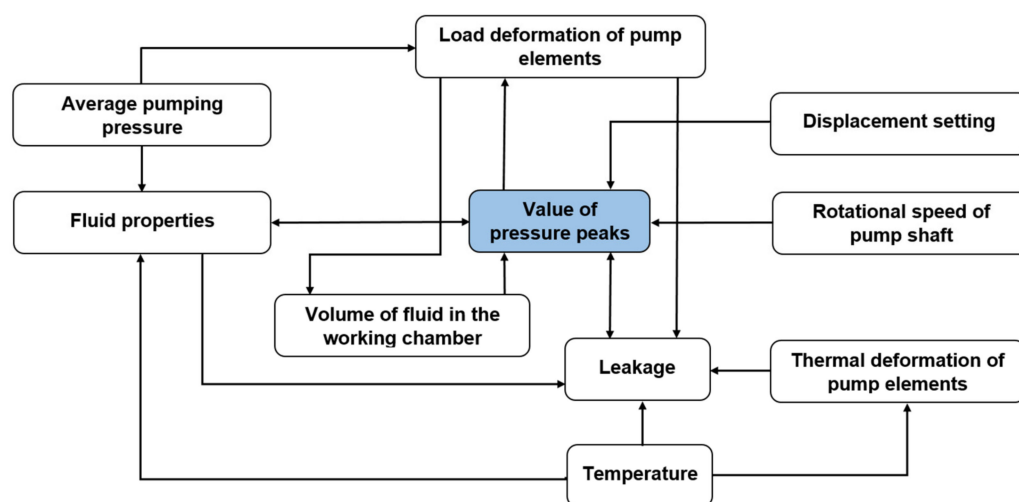


Figure 6. Factors affecting the value of the pressure peaks in the PWK pump.

This article will focus on the impact of the following fluid properties:

- density;
- viscosity;
- compressibility;
- aeration.

The influence of the operational parameters, such as rotational speed, pumping pressure or displacement setting, is described in detail in other publications [12,15,16].

2. Methods and Models

To assess the effect that fluid properties have on the pressure peaks in working chambers of the PWK pump, two research methods were used: an experiment and a numerical simulation. The experiment provided the reference data used to validate the mathematical model used in the numerical simulation.

2.1. Experiment Description

The experiment was conducted in a laboratory of hydraulics using a 70 kW test stand (Figures 7 and 8). The test stand was equipped with a 2000 L oil tank and temperature stabilization system, which guaranteed stable test conditions. It also allowed changing and maintaining a stable oil temperature within the range from 25 °C to 60 °C.

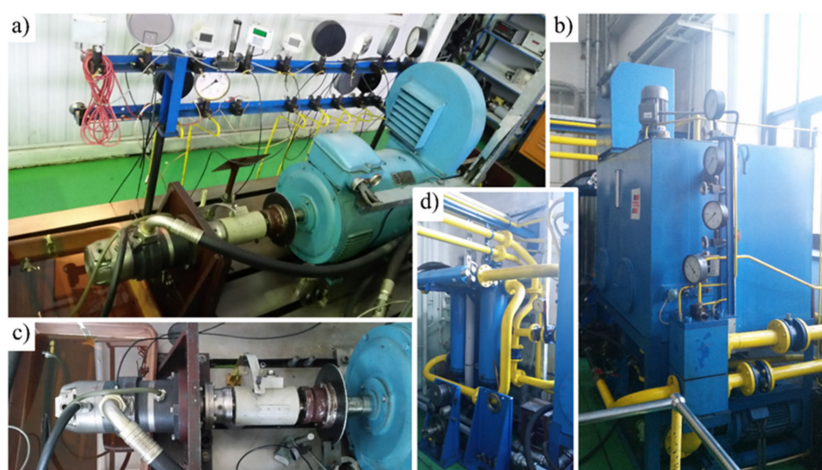


Figure 7. Hydraulic test stand at Gdansk University of Technology [12]: (a) driveline and pressure measurement equipment; (b) tank; (c) pump and mechanical parameter measurement equipment; (d) coolers and heaters.

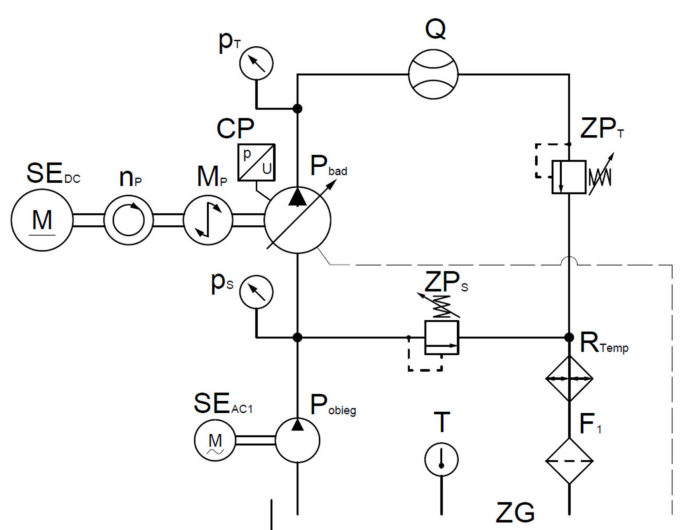


Figure 8. Test stand hydraulic scheme: P_{bad} —tested pump; P_{obieg} —preliminary pump; P_{wir} —auxiliary pump; SE—electric motors; ZP—pressure relief valves; ZG—main tank; R_{Temp} —heat exchanger; F—filters; n_p —tachometer; M_p —torque meter; p—manometers; CP—internal pressure sensor; T—temperature sensor; Q—flow meter.

To measure the value of the pressure peaks, an internal piezoelectric pressure sensor (Figure 9a) was used. It was connected to a working chamber with channels marked with purple color (Figure 9b). The results were recorded with an NI USB-6210 data acquisition (DAQ) module and processed using the “Press-kor” program [12,17]. The obtained results had the form presented in Figure 5. The type and class of measurement equipment used in the experiment was specified in Table 1.

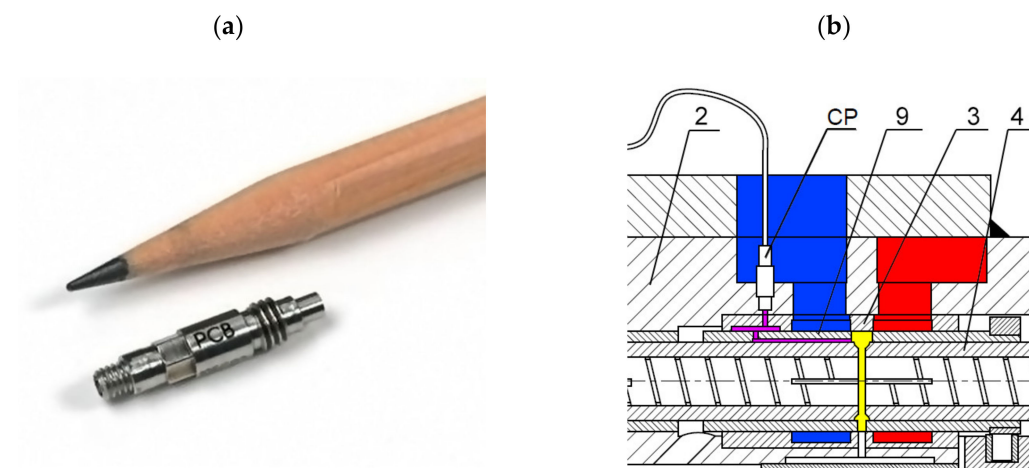


Figure 9. Piezoelectric pressure sensor and its localization inside the pump: 2—body; 3—socket; 4—piston; 9—commutation tube; CP—internal pressure sensor. (a) piezoelectric pressure sensor (b) pressure sensor localization.

Table 1. Specification of the measurement equipment used in the test stand.

No.	Measured Value	Measuring Instrument	Class of the Instrument	Measuring Range	Precision/Sensitivity	Max Uncertainty
1	Pressure at suction channel	MPS-02 manometer	0.2	2.4 MPa	0.001 MPa	0.006 MPa
2	Pressure at pumping channel	HBM manometer	0.2	50 MPa	0.05 MPa	0.15 MPa
3	Pressure at pump's chamber	M105C22 piezoelectric sensor	n/a	34.47 MPa/4888 mV	6.894 kPa/97.43 μ V	437.8 kPa/59.56 mV
		PA-3000 signal amplifier	n/a	20 V	n/a	72.5 mV
		NI-6210 DAQ module	n/a	−10÷10 V	0.306 mV	0.402 mV
4	Flow rate	PT-200 flowmeter	0.2	200 dm ³ /min	0.01 dm ³ /min	0.41 dm ³ /min
5	Output torque	HBM torque meter	0.2	500 Nm	0.01 Nm	1.01 Nm
6	Rotational velocity of pump shaft	Incremental encoder	n/a	3000 RPM	1 RPM	1 RPM
7	Oil temperature	Thermocouple	1.0	70 °C	1 °C	1.7 °C
8	Time	Quartz clock of NI-6210 DAQ module	n/a	3 s	50 ns	no data

Only the impact of the fluid viscosity could be properly tested experimentally, because it is the only fluid property that can be significantly changed without replacing the fluid inside the tank. The viscosity changes its value with the temperature, when density and aeration remain relatively constant. Temperature's impact on the bulk modulus is not

negligible, but still significantly smaller than on viscosity (Figure 10). Therefore, the test could be described as explicit.

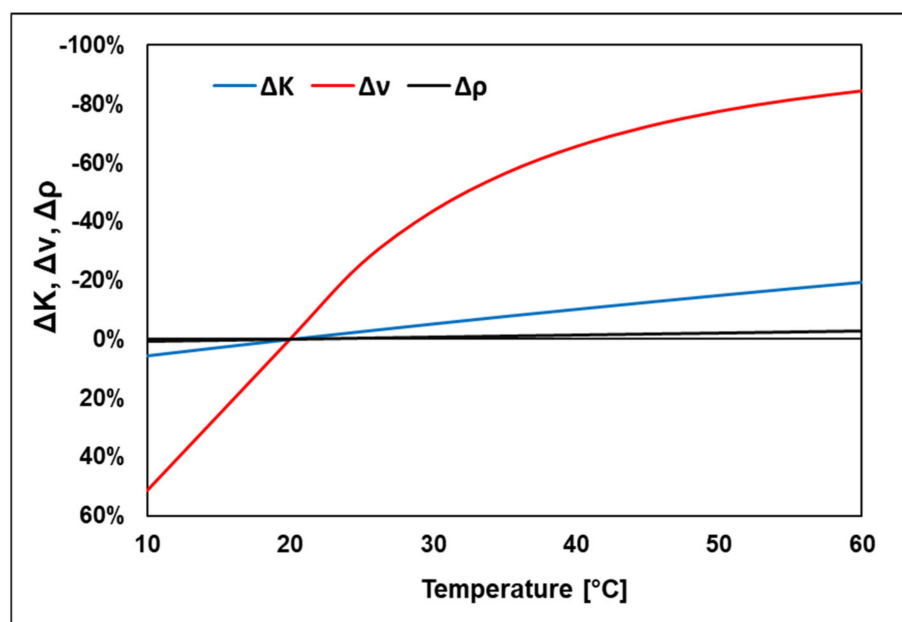


Figure 10. Influence of fluid (mineral oil) temperature on its properties: ΔK -bulk modulus change; Δv -kinematic viscosity change; $\Delta \rho$ -density change (reference values measured at normal conditions).

To experimentally verify the influence of the properties other than viscosity, usage of different fluids, such as synthetic or water-based fluids, would be necessary; still, the test would not be explicit, because with the fluid replacement all its properties would be significantly changed.

2.2. Mathematical and Partial CFD Models

To separate and define the influence of particular properties on the pressure peak value, the numerical model of the pressure peak phenomenon was prepared. It was used to simulate the pressure peaks value under conditions that would be hard to measure in the experiment.

The model is based on the definition of the adiabatic, tangent fluid bulk modulus K_A [18]:

$$K_A = -V_0 \left[\frac{dp}{dV} \right]_A \quad (2)$$

where:

dp —elementary pressure change in the chamber caused by the elementary volume change dV ;

V_0 —initial volume of the chamber at the beginning of the compression process.

The selection of the adiabatic bulk modulus was dictated by the rapidness of the process. It is assumed that the adiabatic bulk modulus would be more appropriate to describe the process lasting milliseconds, which is too brief to develop significant heat exchange than the isothermal bulk modulus, which is considered more desirable in long-lasting processes maintaining a constant temperature. The Equation (2) was used in the numerical model where the calculations were made with a very small iteration step. Therefore, it is considered more desirable for the modulus K_A to give more accurate results around a certain point rather than over a wide range. This feature distinguishes the tangent modulus from the secant and therefore it was selected for further calculations.

The Equation (2) was transformed into the following equation:

$$\Delta p_i = K_{Ai} \left(1 - \frac{V_{ki}}{V_{oi}} \right) \quad (3)$$

where the index i was added to highlight the variables changing iteratively; V_{oi} and V_{ki} are the volumes of the chamber at the beginning and the end of the iteration, respectively; and Δp_i is a pressure change during one iteration.

2.2.1. Fluid Bulk Modulus and Aeration

Fluid bulk modulus is extensively featured in the literature [12,18,19] and there are at least several empiric equations defining its value. For the needs of this article, the Equation (4) [19] describing the secant adiabatic bulk modulus \bar{K}_A was selected:

$$\bar{K}_{Ai} = \left\{ [1.57 + 0.15 \log(v_{20})] 10^{0.0024(20-\tau)} \right\} 10^3 + 5.6 p_i [\text{MPa}] \quad (4)$$

where:

v_{20} —kinematic viscosity in standard conditions (mm^2/s);

τ —temperature ($^{\circ}\text{C}$);

p_i —pressure in chamber at the beginning of the iteration (MPa).

To convert secant \bar{K}_{Ai} to tangent K_{Ai} , differential Equation (5) [18] was used:

$$K_{Ai} = \frac{\bar{K}_{Ai}(\bar{K}_{Ai} - p_i)}{\bar{K}_{Ai} - p_i \frac{d\bar{K}_{Ai}}{dp_i}} \quad (5)$$

resulting in Equation (6), which was used to calculate the sample hydraulic oil characteristics presented in Figure 11:

$$K_{Ai} = [1.57 + 0.15 \log(v_{20})] 10^{0.0024(20-\tau)+3} + 10.2 p_i + \frac{2576 p_i^2}{[1.57 + 0.15 \log(v_{20})] 10^{0.0024(20-\tau)+5}} \quad (6)$$

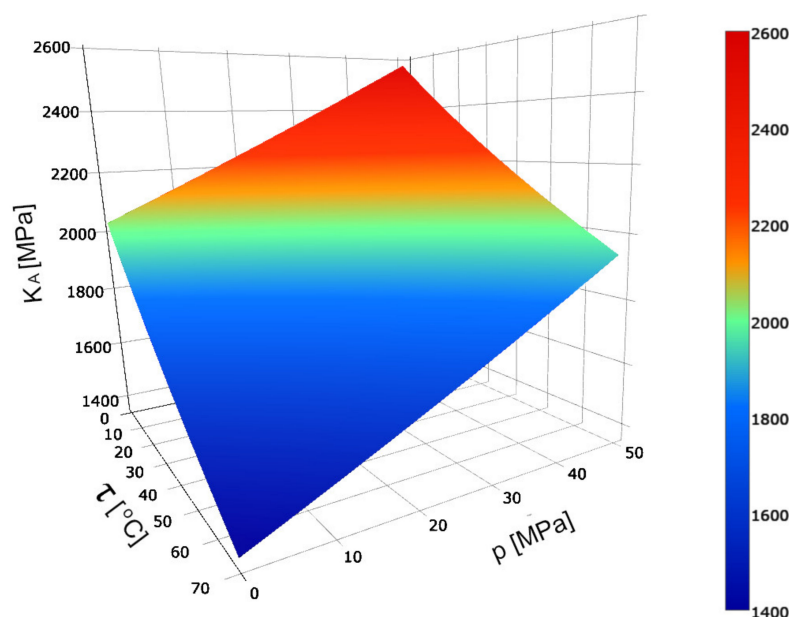


Figure 11. Characteristics of the adiabatic, tangent bulk modulus K_A as a function of pressure p and temperature τ for Total Azolla ZS 46 oil [12].

Equation (6) does not include aeration of the hydraulic fluid. Depending on the type of fluid, the content of air may vary from 1 to 5%. However, full deaeration of fluid is difficult to achieve. Therefore, it is necessary to include the air content in further calculations. The volumetric fraction of the entrained air is defined by Equation (7) as factor X_z :

$$X_z = \frac{V_G}{V_C + V_G} \quad (7)$$

where:

V_G —volume of the gas phase in standard conditions;

V_C —volume of liquid phase in standard conditions.

Many models describing the value of modulus K_A as a function of factor X_z are presented in the literature [18,19]. These models can be divided into two groups, depending on the definition of the compression process. The first group is based on the ideal gas law, assuming that the air mass in the gas phase remains constant during the compression process. This group includes the following:

- Merritt model;
- Nykanen model;
- Cho and Feldman models (each gives the same result).

The second group is based on the ideal gas law, but also includes the partial or full dissolution of air in the oil during pressure rise. This group includes models such as the

- Yu model;
- Ruan–Burton model.

The value of the K_A modulus defined by the models mentioned above is presented in Figure 12. Additionally, for comparison the secant modulus \bar{K}_A and tangent modulus K_A were added to Figure 12. Cho's, Feldman's and Yu's models give the same results.

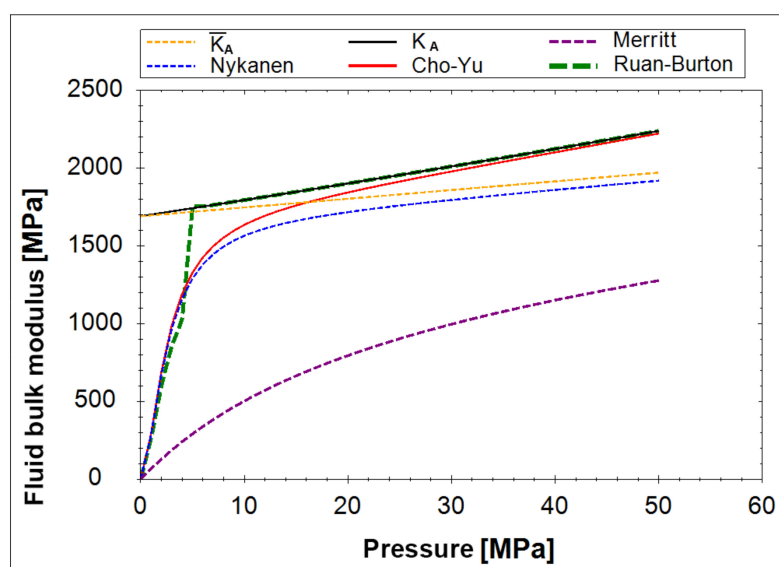


Figure 12. Comparison of the bulk modulus models for Total Azolla ZS 46 oil.

Model Cho was used in further calculations because it showed satisfactory convergence with the research results [20] and has a relatively simple mathematical description with a small number of factors defining it. Model Cho is described by the following equation:

$$K_{Choi} = \frac{(1 - X_z) + \left(\frac{p_n}{p_i}\right)^{\frac{1}{k}} X_z}{\frac{X_z}{k \cdot p_i} \left(\frac{p_n}{p_i}\right)^{\frac{1}{k}} + \frac{1 - X_z}{K_{Ai}}} \quad (8)$$

where:

k —polytrophic exponent;

p_n —normal pressure (1013.25 hPa).

K_{Choi} , including aeration, can substitute K_{Ai} in Equation (3).

2.2.2. Leakage from the Working Chamber

Equation (3) is still oversimplified, because it does not include any leakage out of the cut-off chamber. Therefore, the volume of leakage V_{Li} was added to the V_{ki} component, formulating the following equation:

$$\Delta p_i = K_{Choi} \left(1 - \frac{V_{ki} + \Delta V_{Li}}{V_{oi}} \right) \quad (9)$$

The volume of leakage can be defined as

$$\Delta V_{Li} = Q_{Li} \Delta t_i \quad (10)$$

where:

Q_{Li} is the leakage flow;

Δt_i is the time increment.

There are three main sources of leakage from the cut-off working chamber (11) (Figure 13):

- Flow through the piston hydrostatic supports, Q_{hs} ;
- Flow through the annular gaps between the pistons and commutation tube, Q_t ;
- Flow through the gap in the commutation widow, Q_{ok} .

$$Q_{Li} = Q_{hs} + Q_t + Q_{ok} \quad (11)$$

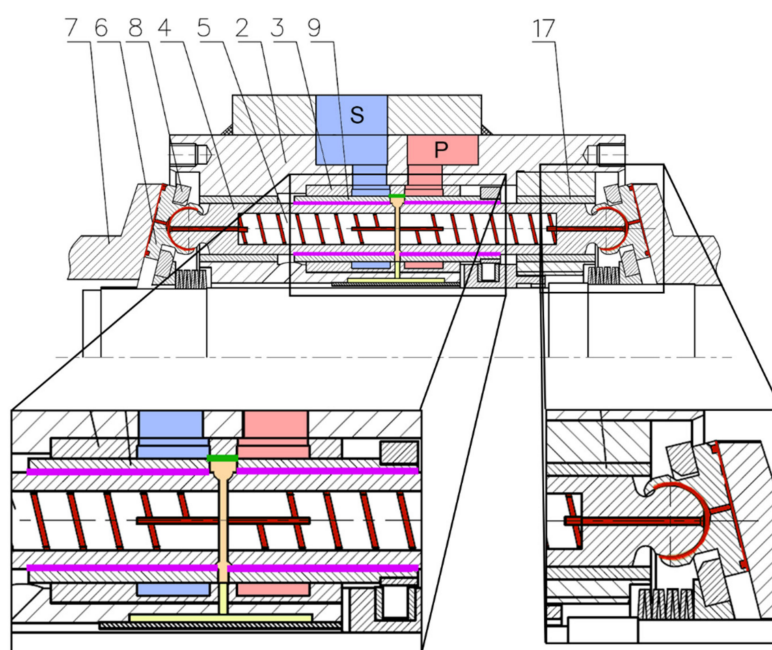


Figure 13. Localization of the leakage sources [12]: red—flow through the hydrostatic supports; purple—flow through the annular gaps between the pistons and commutation tube; green—flow through the gap in the commutation widow; 2—body; 3—socket; 4—piston; 5—spiral choke; 6—slipper; 7—swash-plate; 8—separator plate; 9—commutation tube; 17—guiding tube.

The first source of the leakage taken into consideration is the hydrostatic support in the slipper. The flow through the support equals the flow Q_{hs} through the spiral choke (Figure 14), which is described in [12,21].

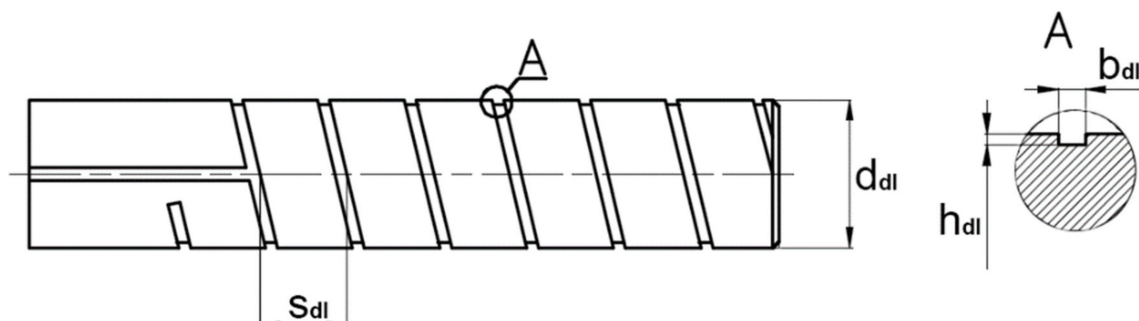


Figure 14. Spiral choke [5].

The flow through the choke is almost laminar and given by the following equation:

$$Q_{hs} = 0.87 \frac{\Delta p_{ch} \cdot h_{dl}}{\nu \cdot \rho \cdot L_{dl}} \quad (12)$$

where Δp_{ch} is an unknown pressure drop in spiral choke, and L_{dl} is the length of a screw line. Forces equilibrium Equation (13), formulated based on the dimensions and forces presented in Figure 15, is a starting point for calculations of Δp_{ch} .

$$F_t = F_{phs} \cdot \cos \xi \quad (13)$$

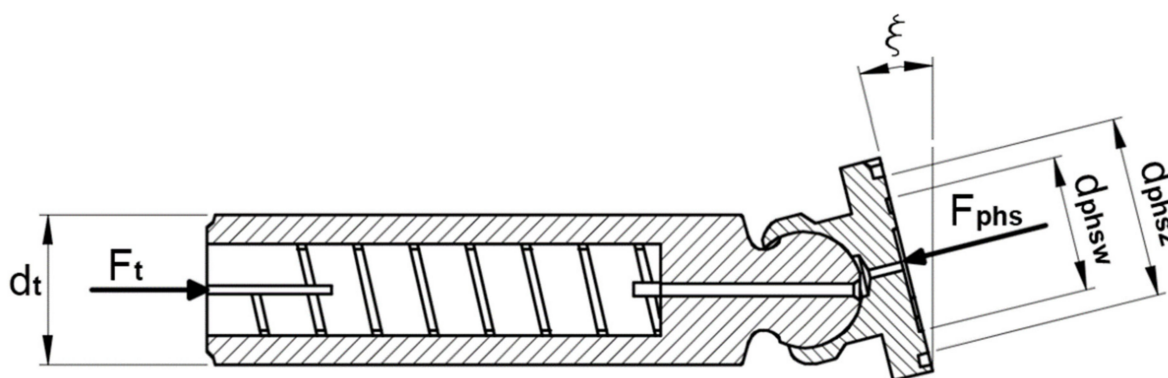


Figure 15. Load distribution on the piston and slipper [5].

Force F_t is generated by the pressure p_i inside the working chamber and described by the following equation:

$$F_t = p_i \cdot \frac{\pi d_t^2}{4} \quad (14)$$

Force F_{phs} is generated by the pressure gradient under the slipper and given by the following equation [22,23]:

$$F_{phs} = p_{hs} \frac{\pi (d_{phsz}^2 - d_{phsw}^2)}{8 \ln \left(\frac{d_{phsz}}{d_{phsw}} \right)} \quad (15)$$

where p_{hs} is the pressure in the outlet of the spiral choke. The p_{hs} is calculated using Equation (16):

$$p_{hs} = p_i \frac{2d_t^2 \cdot \ln\left(\frac{d_{phsz}}{d_{phsw}}\right)}{\left(d_{phsz}^2 - d_{phsw}^2\right) \cos \xi} \quad (16)$$

which was formulated by transforming Equation (13), in which forces F_t and F_{phs} were substituted with Equations (14) and (15).

Knowing that the pressure drop in the spiral choke is the difference between the pressure inside the working chamber p_i and the pressure p_{hs} , Equation (17) may be formulated.

$$\Delta p_{ch} = p_i - p_{hs} \quad (17)$$

From Equations (16) and (17), Equation (18) was derived.

$$\Delta p_{ch} = p_i \left[1 - \frac{2d_t^2 \cdot \ln\left(\frac{d_{phsz}}{d_{phsw}}\right)}{\left(d_{phsz}^2 - d_{phsw}^2\right) \cos \xi} \right] \quad (18)$$

Equation (18) can be substituted into Equation (12), which is used to calculate the leakage flow, Q_{hs} .

The second leakage source is the annular gap between the piston and the commutation tube (Figure 2). It is not fully known if the gap is central or skewed. The skewness of the gap may be caused by the situation presented in Figure 16. The compounds of the forces from the swashplates (7), acting perpendicularly on the pistons (4), displace them. Since the pistons (4) are paired and are sliding inside the single commutation tube (9), their skewness cannot be compensated for by the displacement of the tube (9). However, some authors declare that the pistons are centered by the fluid film pressure acting on the pistons inside the tube. Probably, the pistons are only partially skewed thanks to the fluid film pressure and tightly fitted guiding tubes (17) (Figure 2), but not entirely.

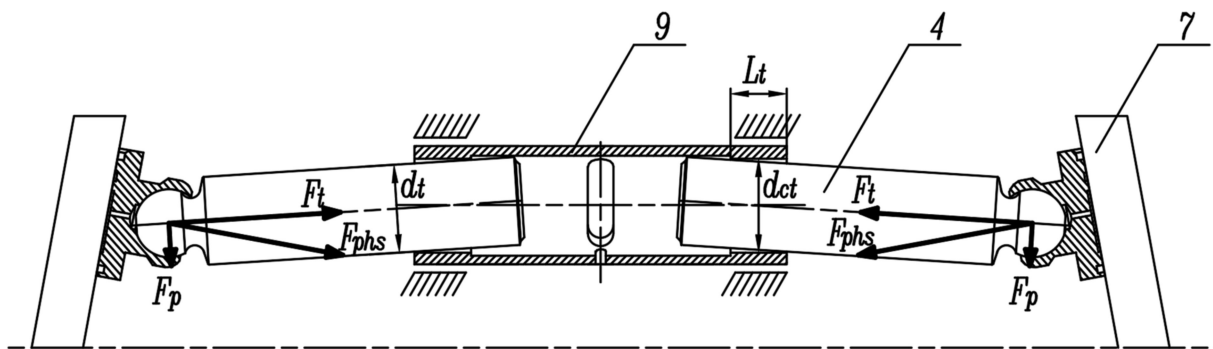


Figure 16. Skewed annular gap between the pistons (4) and commutation tube (9).

Flow through the partially skewed annular gap can be expressed using the following equation [24–26]:

$$Q_{ti} = \frac{p_i \cdot \pi \cdot d_t \cdot h_t^3}{12 \cdot \nu \cdot \rho \cdot L_t} \cdot \alpha \quad (19)$$

where:

- α —the skewness coefficient, varying from 1 to 1.38;
- h_t —average height of the annular gap.

$$h_t = \frac{d_{ct} - d_t}{2} \quad (20)$$

The last important location of the leakage from the chamber is the commutation window (Figure 13). Although the commutation bridge is 0.5 mm wider than the commutation window and overlaps it completely, it is known that the leakage flow through the window has the biggest value of all mentioned before. The circular gap around the window is the shortest of all and relatively wide, which causes such as high leakage through it. The simplified shape of the gap is presented in Figure 17.

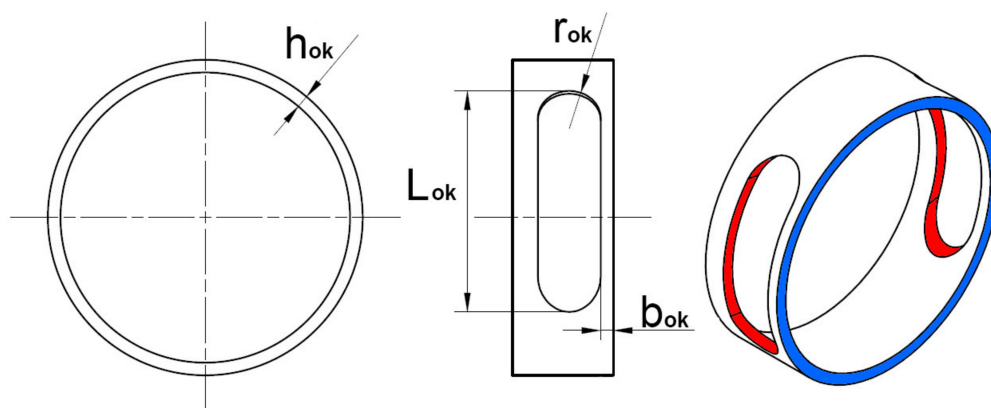


Figure 17. Simplified geometry of a gap in the commutation window: red—inlet; blue—outlet.

The gap changes its geometry because the window is moving with the commutation tube. Therefore, the simulation of the flow through the gap was needed. Detailed description of the CFD model can be found in [12]. The results of the simulation are presented in Figure 18. Figure 18a presents the influence of the pressure difference between the inlet and outlet of the gap on the leakage flow. Figure 18b presents how the leakage flow is influenced by a change in dimension b_{ok} (Figure 17).

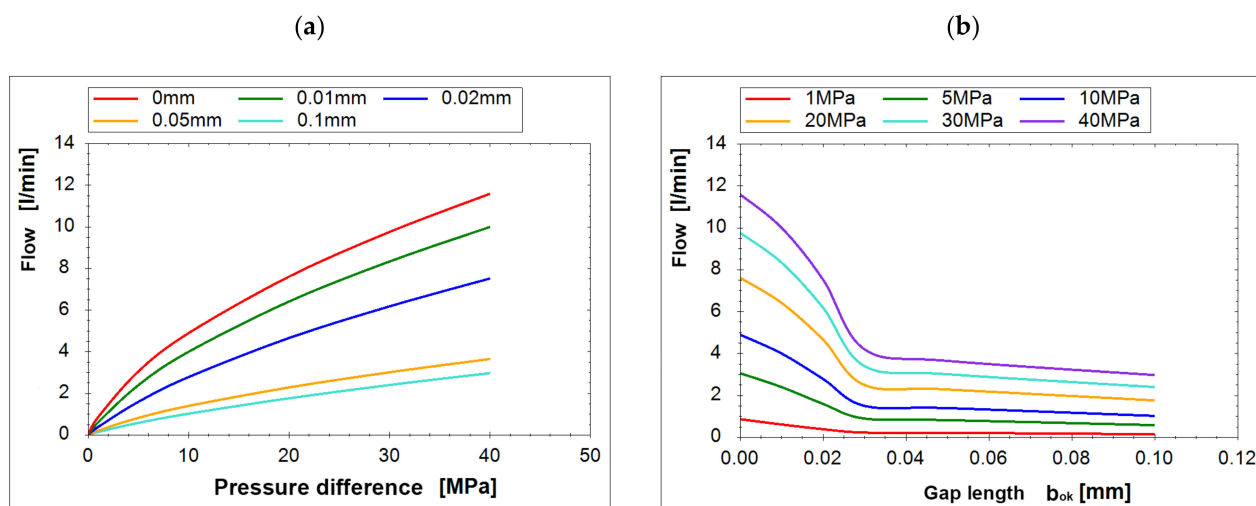


Figure 18. Influence of the pressure difference between the inlet and outlet of the gap and the gap length on the leakage flow: (a) characteristic of the flow as a function of pressure difference Δp for different gap lengths b_{ok} ; (b) characteristic of the flow as a function of gap length b_{ok} for different pressure differences Δp .

The presented results show the sudden change in flow type. At a gap length b_{ok} lower than $b_{oko} = 0.02$ mm, turbulent flow is the dominating type of flow, and when the gap is longer than 0.02 mm, the flow becomes more laminar. The following equation has been formulated to model this phenomenon:

$$Q_{ok} = Q_{lam} \cdot f(b_{ok}) + Q_{tur}[1 - f(b_{ok})] \quad (21)$$

where:

Q_{lam} is the laminar flow component;

Q_{tur} is the turbulent flow component;

$f(b_{ok})$ represents the transition function described by the following logistic function:

$$f(b_{ok}) = \frac{1}{1 + e^{-18(\frac{b_{ok}}{b_{okr}} + 1)}} \quad (22)$$

The laminar component of flow was described as through a gap presented in Figure 19. The shown gap was divided into an infinite number of planar gaps, marked in Figure 19 in red.

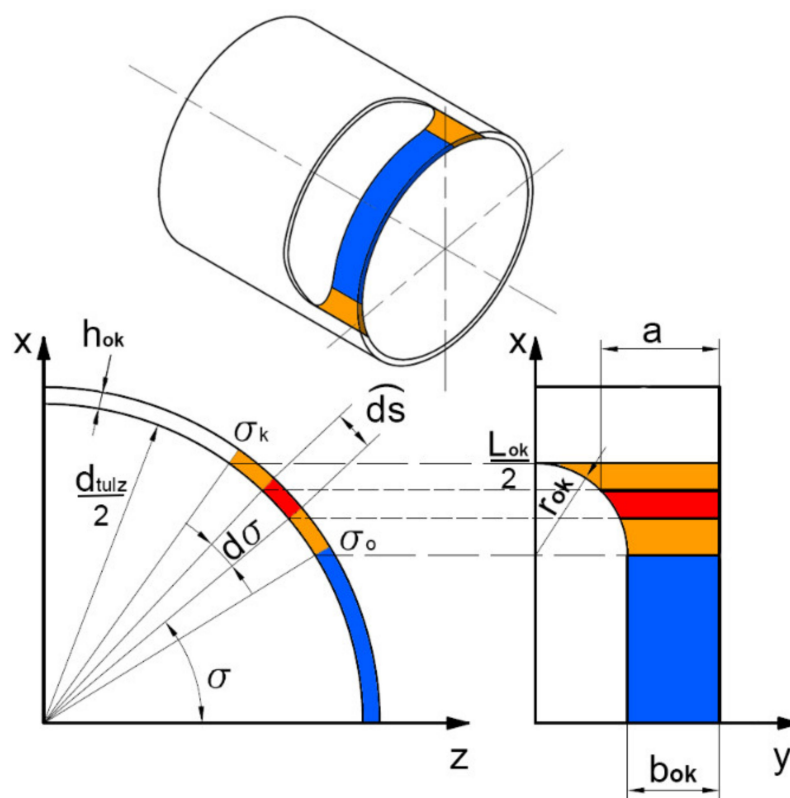


Figure 19. Graphical representation of the model of the commutation window gap.

The flow dQ_{lam} through the infinitesimal gap is described by the following equation:

$$dQ_{lam} = \frac{\Delta p \cdot h_{ok}^3}{12 \cdot \nu \cdot \rho \cdot a} \hat{ds} \quad (23)$$

where:

ν —kinematic viscosity;

ρ —density;

After mathematical integration, Equation (24) describing Q_{lam} was obtained:

$$Q_{lam} = \frac{\Delta p \cdot d_{tulz} \cdot h_{ok}^3}{12 \cdot \nu \cdot \rho} \left[\frac{\sigma_o}{b_{ok}} + \int_{\sigma_o}^{\sigma_k} \frac{d\sigma}{b_{ok} + r_{ok} - \sqrt{r_{ok}^2 - \left(\frac{d_{tulz}}{2} \cdot \sin \sigma - \frac{L_{ok}}{2} + r_{ok} \right)^2}} \right] \quad (24)$$

Since the integral in (24) does not have an analytical solution, it was solved using numerical methods.

The turbulent component of the flow Q_{tur} was calculated using

$$\Delta p = \zeta_{ok} \cdot \rho \frac{c_{ok}^2}{2} \quad (25)$$

where:

ζ_{ok} —is the local resistance coefficient [12];

c_{ok} —is an average flow velocity calculated using

$$c_{ok} = \frac{Q_{tur}}{h_{ok} \cdot \sigma_k \cdot d_{tulz}} \quad (26)$$

Using substitution and transformation, Equation (27) is obtained:

$$Q_{tur} = h_{ok} \cdot \sigma_k \cdot d_{tulz} \sqrt{\frac{2\Delta p}{\zeta_{ok} \cdot \rho}} \quad (27)$$

To calculate the coefficient ζ_{ok} and validate the mathematical model (21), a steady state CFD analysis was conducted in ANSYS CFX. The domain presented in Figure 20a consists of four separate parts:

- peripheral channel (purple);
- gap between the commutation tube and the socket (transparent grey);
- two commutation windows (yellow).

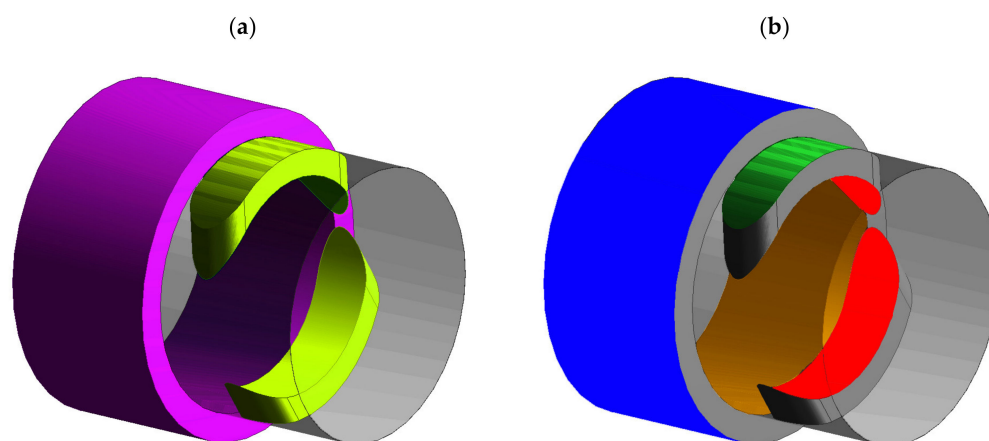


Figure 20. Domain geometry and border conditions. (a) Parts of domain: purple—peripheral channel; transparent grey—gap between the commutation tube and the socket; yellow—commutation windows. (b) Border conditions: red—inlet; blue—outlet; green and orange—interfaces.

In Figure 20b, the boundary conditions are marked. The inlet (red) boundary condition was the constant pressure inside the working chamber. Constant pressure opening was assigned to the outlet (blue). The peripheral outlet was a simplification, because in the real pump there are two radial channels connected to the peripheral channel. The preliminary tests proved that they do not affect the flow in the analyzed gap; therefore, they were omitted. Two interfaces were created to connect the separate parts of the domain. The orange interface connected the peripheral channel and the gap between the commutation tube and the socket. A green interface connected the gap and commutation window. The grey parts of the model in Figure 20b were no-slip walls. The model allowed to change the gap dimensions, inlet and outlet pressures, and the fluid properties.

The domain was discretized into computational mesh consisting of the hexahedral volumes presented in Figure 21. Each part was divided so that the mesh becomes denser the closer it is to the analyzed gap, which significantly improved the solution and did not extend the computation time excessively.

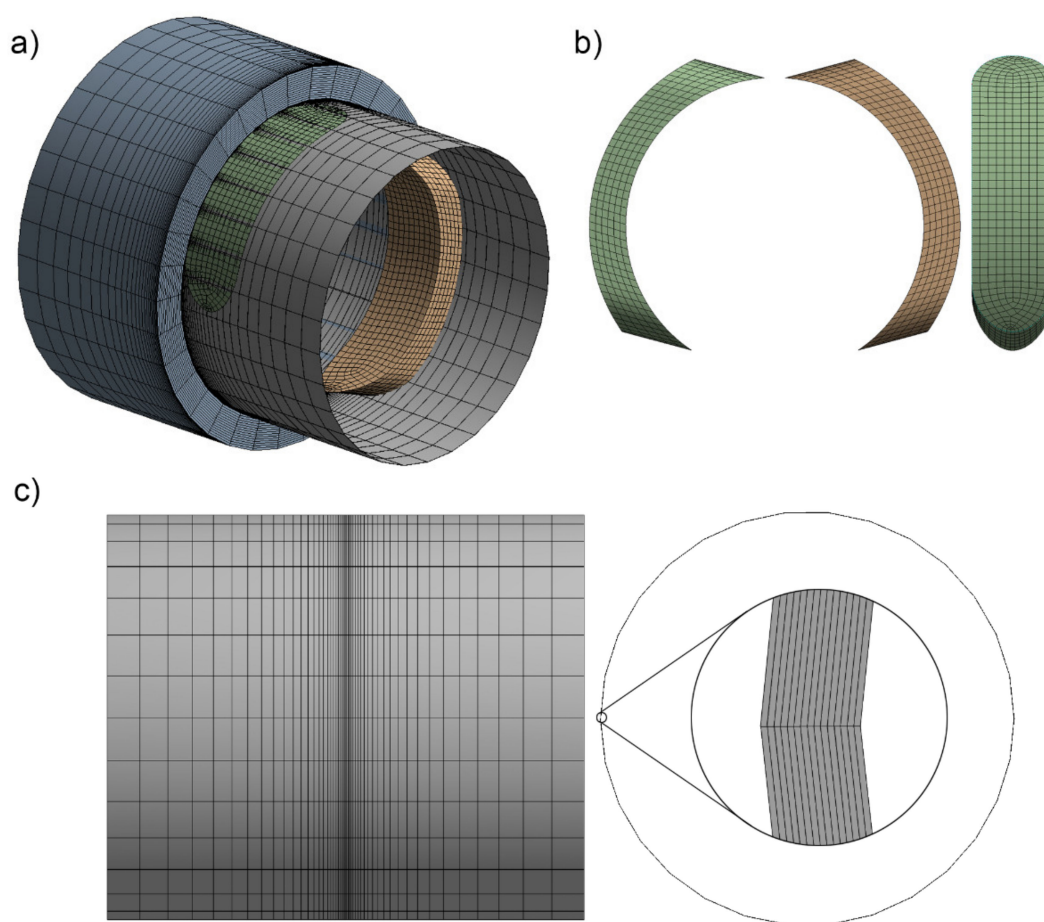


Figure 21. Discretization of the domain into computational mesh: (a) complete model; (b) commutation windows; (c) gap between the commutation tube and socket [26].

To simulate the flow in the gap: $k-\omega$, $k-\varepsilon$ and Shear Stress Transport (SST) turbulence models were tested; however, the solver was able to converge in all cases only when using the SST model. In some cases, where the solver converged, all models gave similar results. Therefore, the SST model was utilized in further calculations.

A comparison of the results obtained from (21) and the CFD model is presented in Figure 22. The difference between the model and simulation does not exceed 10% if the pressure does not rise over 30 MPa, which is acceptable.

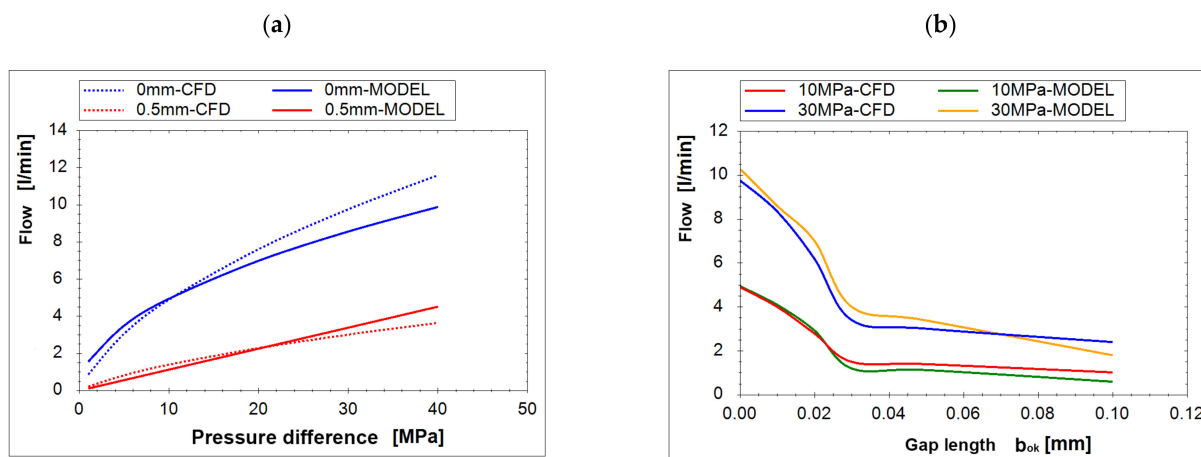


Figure 22. Comparison of the characteristics obtained from the CFD simulation and (21): (a) characteristic of the flow as a function of the pressure difference Δp for different gap lengths b_{0k} ; (b) characteristic of the flow as a function of the gap length b_{0k} for different pressure differences Δp .

2.3. Discrete Model of the Compression Process

All the above equations were used to prepare a discrete model of the compression process inside the pump's working chamber (Figure 23).

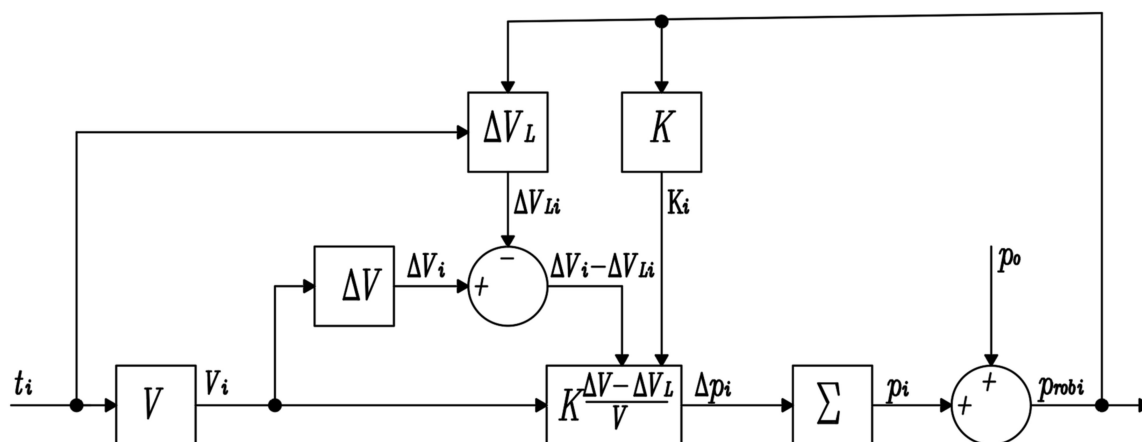


Figure 23. Simplified block diagram of the discrete simulation model of the compression process.

In this model, time t_i and pumping pressure p_o were the input parameters. At $t_o = 0$ s the commutation window became fully closed and the compression process began. The compression process was divided into equal timesteps, and for every timestep the actual volume of the working chamber V_i was calculated in block V. Additionally, in block ΔV , the elementary change in volume for every timestep was calculated using the following formula:

$$\Delta V_i = V_i - V_{i-1} \quad (28)$$

The ΔV_L block includes Formula (10) and calculates the elementary leakage volume ΔV_{Li} for every timestep. Block K includes Equation (8) and is used to calculate the bulk modulus K_i at time t_i . Using Equation (9), block $K \frac{\Delta V - \Delta V_L}{V}$ calculates the elementary pressure change Δp_i for every timestep. All pressure changes Δp_i are being summed up in block Σ , resulting in an actual pressure peak value p_i calculated at time t_i . The sum of p_i and p_o is the actual value of the pressure in the working chamber p_{robi} . The pressure p_{robi} is used in an algebraic loop to calculate ΔV_{Li} and K_i in blocks ΔV_L and K. The model was implemented in the Matlab Simulink environment. It allowed to change the geometrical parameters of the pump, the operational parameters, such as pumping pressure or displacement, and of course all the earlier mentioned fluid properties. The results of the simulation using this discrete model are displayed as time domain graphs (Figure 24), presenting the change in pressure in the cut-off working chamber or as a value of a maximal registered pressure.

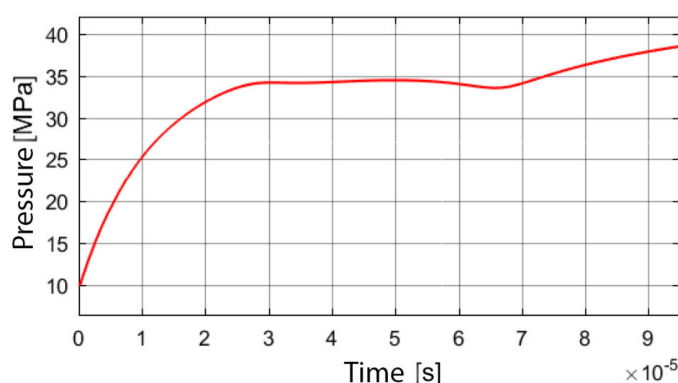


Figure 24. Sample result of the simulation using the Simulink discrete model.

Since the results presented as series of time domain graphs would be very hard to interpret in the context of fluid properties, in the following part of the article the results will be elaborated upon and presented in another form.

3. Results of the Experiment

Only the impact of viscosity could be measured using the laboratory methods because it is the only parameter that can be significantly changed by changing the fluid temperature, not by changing the fluid itself. The results are presented in Figure 25. It is easy to see that a rising viscosity always increases the pressure peak value, despite the changes in pumping pressure or rotational speed. This means that the leakage flow Q_{Li} in Equation (10) decrease with the viscosity and the pressure inside the working chamber is not unloaded as efficiently as it was, causing a significant pressure peak rise.

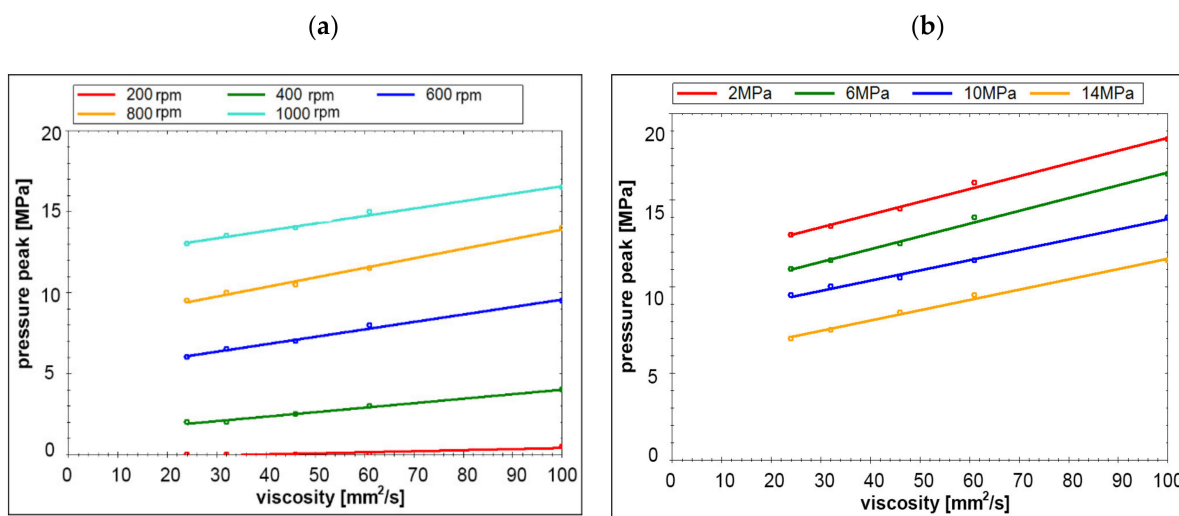


Figure 25. Influence of viscosity on pressure peaks value: (a) measured at a constant pumping pressure of 10 MPa, pump displacement set to 20% of the maximal value and a variable rotational speed; (b) measured at a constant rotational speed, pump displacement set to 20% of the maximal value and a variable pumping pressure.

Since the laboratory research was very limited and not fully explicit because of the temperature-dependent bulk modulus and density, it was mainly used as a reference for the simulation.

4. Results of the Simulation

The results of the simulation were prepared in Matlab Simulink using the discrete model described in Section 2. A series of numerical calculations were conducted to obtain the time domain graphs similar to the one presented in Figure 24. From the time domain graphs the pressure peak value was read and presented in Figure 26. From it, it is clear that the biggest impact on the pressure peaks are the fluid properties that significantly influence flow resistance: viscosity (Figure 26a) and density (Figure 26b). As it was written before, the hydraulic oil viscosity strongly depends on the temperature, which in normal work conditions can vary from $10 \frac{\text{mm}^2}{\text{s}}$ to $250 \frac{\text{mm}^2}{\text{s}}$. It is also possible to use water and water-based liquids as the hydraulic fluid; therefore, the viscosity can drop below $1 \frac{\text{mm}^2}{\text{s}}$. The lower the viscosity is the lower pressure peaks are being predicted, because the increased leakage does not allow to pressurise the liquid in the pump's chambers.

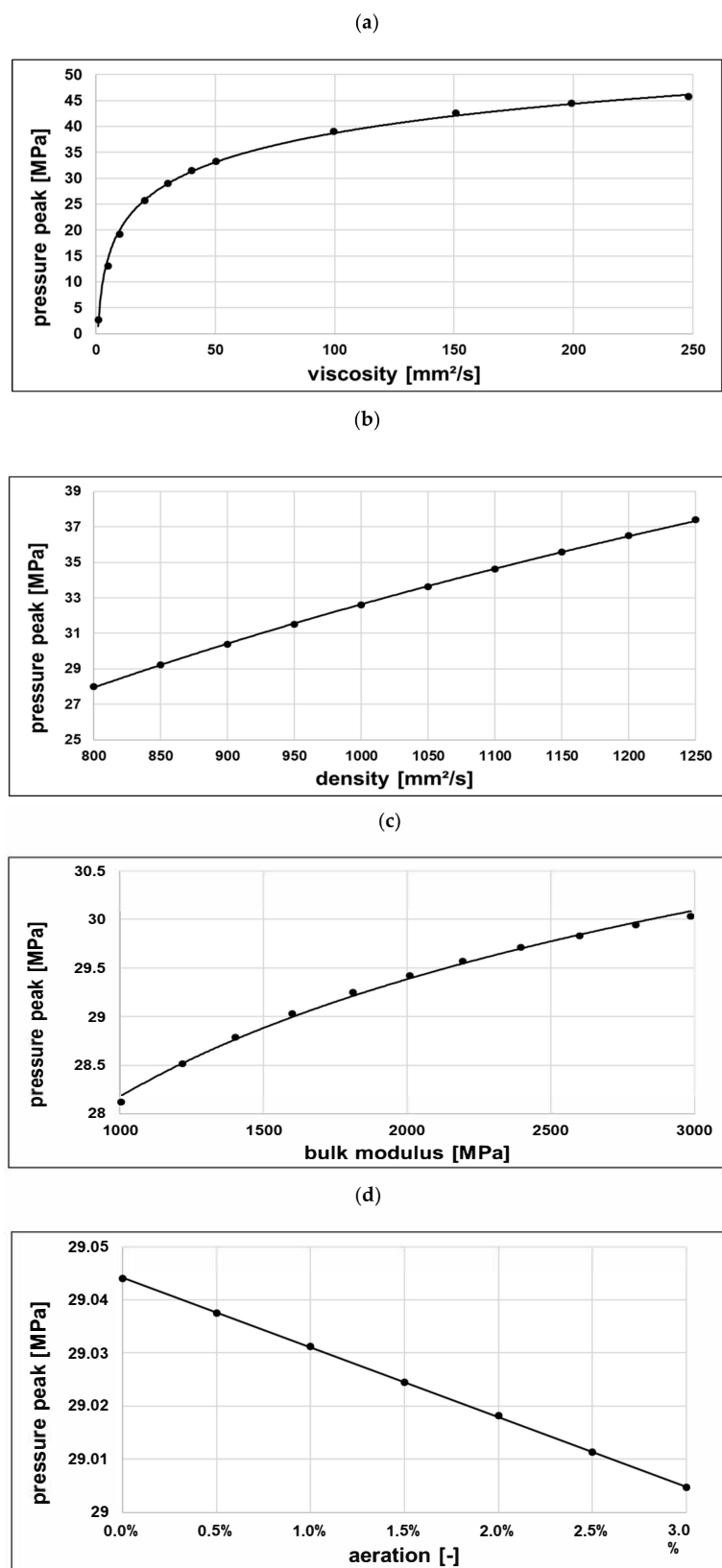


Figure 26. Influence of the properties of hydraulic fluid on the pressure peaks value: (a) influence of viscosity; (b) influence of density; (c) influence of the bulk modulus; (d) influence of aeration. All simulations were conducted with the following settings: pumping pressure $p_o = 10$ MPa, rotational speed $n = 1500$ rpm, and displacement setting $x = 20\%$. All constant fluid parameters were properties of the Total Azolla 46 oil, calculated at a temperature of 50°C and at 0% aeration.

Density also strongly affects the pressure peaks value; however, to significantly alter the density, it is necessary to change the fluid in the whole hydraulic circuit. The predicted effect of such a change is presented in Figure 26b. The density of the more commonly used fluids can vary from $840 \frac{\text{kg}}{\text{m}^3}$ for hot mineral oil to $1261 \frac{\text{kg}}{\text{m}^3}$ for glycerine.

What was unexpected, was that the bulk modulus had a relatively low impact on the pressure peaks value. The effect of the bulk modulus change from 1000 MPa to 3000 MPa (Figure 26c) is lower than 10%. Since aeration affects the bulk modulus, its impact on the pressure peaks is even lower (Figure 26d). In normal working conditions, when the fraction of undissolved air does not exceed 3%, the aeration influence is negligible.

5. Discussion and Conclusions

As suggested earlier, the results of the experiment (Figure 25) may not be fully explicit, since during the experiment the change in viscosity was caused by the temperature change. The temperature also affected the bulk modulus and density values (Figure 10). To validate the results of the experiment, a simulation was conducted using models in which all fluid properties were temperature dependent or only viscosity was temperature dependent. The results of this validation are presented in Figure 27. What is easy to notice, is the change in bulk modulus and density caused by the temperature variation did not affect the result significantly. Especially at temperatures below 40 °C, this impact could be described as negligible. Therefore, it is possible to say that the experiment, which was conducted in temperatures varying from 25 °C to 55 °C, presents a true influence of viscosity on the pressure peaks value.

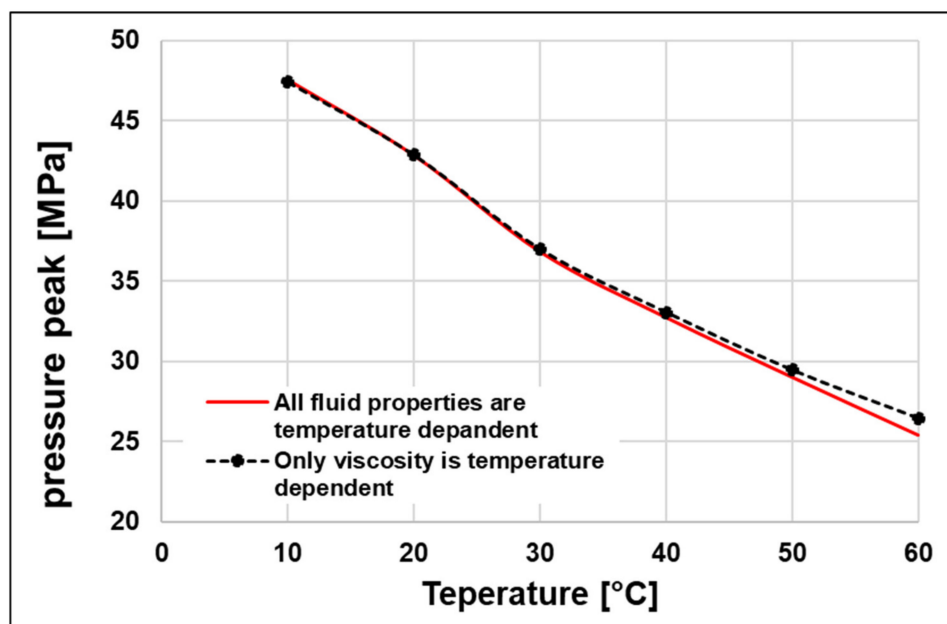


Figure 27. Comparison of the pressure peaks values predicted using a model in which only viscosity was temperature dependent and model in which all fluid properties were temperature dependent.

To verify the model (Figure 23), the results of the experiment and simulation are compared in Figure 28. The model gives better results for lower viscosities and the general error does not exceed 10% of the experiment result value, if the fluid temperature is above 40 °C. It is also noticeable that the model is much more accurate for a lower rotational speed and pumping pressure. However, even for higher values of rotational speed and pumping pressure, the direction of the pressure peak changes is maintained, and the maximal error of the model does not exceed 30% of the measured value.

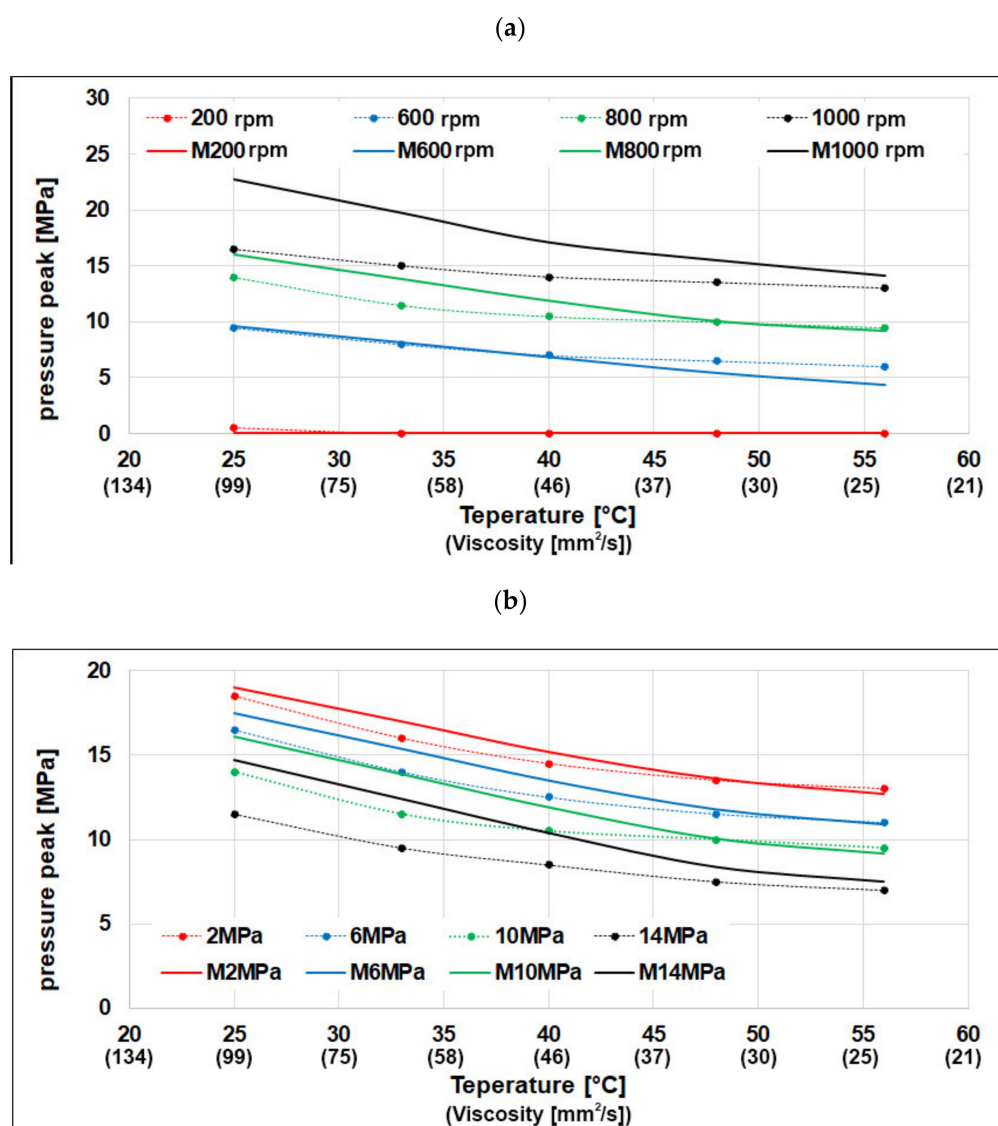


Figure 28. Comparison of the pressure peak values obtained for variable temperatures (viscosity) from the experiment and simulation: (a) obtained at a constant pumping pressure of 10 MPa, displacement setting of 20% and variable rotational speed; (b) obtained at a constant rotational speed, displacement setting of 20% and variable pumping pressure (experiment results are marked with a thicker solid line, and the simulation results are marked with a thinner dotted line).

In articles, such as [27–29], the authors describe the pressure peaks phenomenon in axial piston pumps. However, they concentrate on the design aspects of the problem. They analyzed the impact of the commutation design and the influence of the operational parameters, such as the pumping pressure and rotational speed. Except for fluid viscosity, they did not take into consideration other fluid properties. Nowadays, when a mineral oil is frequently substituted with water- or vegetable oil-based fluids, the impact of the bulk modulus, density or aeration cannot be omitted.

The other group of articles [7,30–33] shows the consequences of using alternative hydraulic fluids on operational parameters such as overall efficiency, leakage and momentum losses, but they do not include the impact of the fluid change on pressure peaks. Most of them concentrate on the fluid and not on its properties; therefore, it is hard to relate the included data to other non-described fluids.

This article presents a new approach to the problem. It shows how specific parameters of the fluid impact the generation of pressure peaks in axial piston pumps; therefore, it can

not only be used as a source of information about commonly used fluids, but also to assess the results of using new, never-tested hydraulic fluids. Additionally, the mathematical models included in the article show the methodology of calculating the compression of the fluid in cut-off chambers of the pump and may be used to assess the leakage in axial piston machines. Future research of the subject will concentrate on pumps with plate commutation and will include pressure-induced deformation of the gaps.

Funding: This research was funded by The National Centre for Research and Development within the framework of program LIDER, grant number LIDER/22/0130/L-8/16/NCBR/2017. Project title: Hydro-mechanical automatic gearbox for agricultural vehicles and heavy machinery. Funding value: 1,197,500.00 PLN.

Institutional Review Board Statement: Not applicable.

Informed Consent Statement: Not applicable.

Data Availability Statement: Data available in a publicly accessible repository. The data presented in this study are openly available in [12,34].

Conflicts of Interest: The author declares no conflict of interest.

References

1. Ivantysyn, J.; Ivantysynova, M.; Ivantysyn, J. *Hydrostatic Pumps and Motors: Principles, Design, Performance, Modelling, Analysis, Control and Testing*; Tech Books International: New Delhi, India, 2003; ISBN 978-81-85522-16-6.
2. Guo, S.; Chen, J.; Lu, Y.; Wang, Y.; Dong, H. Hydraulic Piston Pump in Civil Aircraft: Current Status, Future Directions and Critical Technologies. *Chin. J. Aeronaut.* **2020**, *33*, 16–30. [CrossRef]
3. Kumar, S. *CFD Analysis of an Axial Piston Pump*; Universitat Politècnica de Catalunya: Barcelona, Spain, 2010. [CrossRef]
4. Cieślak, K.; Krogul, P.; Rubiec, A.; Spadło, K. Concept of a Vehicle for Collecting and Transporting Baled Biomass. In Proceedings of the 10th International Conference on Intelligent Technologies in Logistics and Mechatronics Systems, I^{TEL}MS, Panevezys, Lithuania, 21 May 2015; pp. 69–74.
5. Przybysz, M.; Rubiec, A. Simulation Research of Kinematic Discrepancy in Multiaxis Hydrostatic Drive Systems. In Proceedings of the 11th International Conference on Intelligent Technologies in Logistics and Mechatronics Systems, I^{TEL}MS 2016, Panevezys, Lithuania, 28–29 April 2016; pp. 131–140.
6. Sliwinski, P. The Basics of Design and Experimental Tests of the Commutation Unit of a Hydraulic Satellite Motor. *Arch. Civ. Mech. Eng.* **2016**, *16*. [CrossRef]
7. Śliwiński, P. Influence of Water and Mineral Oil on the Leaks in Satellite Motor Commutation Unit Clearances. *Pol. Marit. Res.* **2017**, *24*. [CrossRef]
8. Wu, X.; Chen, C.; Hong, C.; He, Y. Flow Ripple Analysis and Structural Parametric Design of a Piston Pump. *J. Mech. Sci. Technol.* **2017**, *31*, 4245–4254. [CrossRef]
9. Xu, B.; Ye, S.; Zhang, J.; Zhang, C. Flow Ripple Reduction of an Axial Piston Pump by a Combination of Cross-Angle and Pressure Relief Grooves: Analysis and Optimization. *J. Mech. Sci. Technol.* **2016**, *30*, 2531–2545. [CrossRef]
10. Hong, H.; Zhao, C.; Zhang, B.; Bai, D.; Yang, H. Flow Ripple Reduction of Axial-Piston Pump by Structure Optimizing of Outlet Triangular Damping Groove. *Processes* **2020**, *8*, 1664. [CrossRef]
11. Osiecki, A.; Osiecki, L. Hydrostatic Axial Piston Machine. European Patent 0 742 870, 1999.
12. Patrosz, P. Compensation of Pressure Peaks in Variable Displacement Piston Pump with Cam Driven Commutation, (Original title: Kompensacja Skoków Ciśnienia w Pompie Tłoczkowej z Rozrządem Krzywkowym). Ph.D. Thesis, Gdansk University of Technology, Gdansk, Poland, 2017. Available online: https://mostwiedzy.pl/pl/publication/download/1/kompensacja-skokow-cisnienia-w-pompie-tloczkowej-o-zmiennej-wydajnosci-z-rozrzadem-krzywkowym_32490.pdf (accessed on 10 June 2021). (In Polish).
13. Załuski, P. Influence of the Position of the Swash Plate Rotation Axis on the Volumetric Efficiency of the Axial Piston Pumps. *Sci. Tech. Union Mech. Eng.* **2014**, *11*, 12–15.
14. Załuski, P. Experimental Research of an Axial Piston Pump with Displaced Swash Plate Axis of Rotation. In *Advances in Hydraulic and Pneumatic Drives and Control 2020*; Stryczek, J., Warzyńska, U., Eds.; Lecture Notes in Mechanical Engineering; Springer International Publishing: Cham, Switzerland, 2021; pp. 135–145. ISBN 978-3-030-59508-1.
15. Osiecki, L.; Patrosz, P.; Zawistowski, T.; Landvogt, B.; Piechna, J.; Żyliński, B. Compensation of Pressure Peaks in PWK-Type Hydraulic Pumps. *Key Eng. Mater.* **2011**, *490*, 33–44. [CrossRef]
16. Osiecki, L.; Patrosz, P.; Landvogt, B.; Piechna, J.; Zawistowski, T.; Żyliński, B. Simulation of Fluid Structure Interaction in a Novel Design of High Pressure Axial Piston Hydraulic Pump. *Arch. Mech. Eng.* **2013**, *60*, 509–529. [CrossRef]
17. Osiński, P.; Patrosz, P. Badania dynamicznych przebiegów ciśnienia w pompach wyporowych z wykorzystaniem czujników piezoelektrycznych. *Napędy Sterow.* **2016**, *18*, 110–114.

18. Gholizadeh, H.; Burton, R.; Schoenau, G. Fluid Bulk Modulus: A Literature Survey. *Int. J. Fluid Power* **2011**, *12*, 5–15. [[CrossRef](#)]
19. Hodges, P.K.B. *Hydraulic Fluids*; Arnold, J., Ed.; Wiley: London, UK; Wiley: New York, NY, USA, 1996; ISBN 978-0-340-67652-3.
20. Gholizadeh, H. Modeling and Experimental Evaluation of the Effective Bulk Modulus for a Mixture of Hydraulic Oil and Air. Ph.D. Thesis, University of Saskatchewan, Saskatchewan, SK, Canada, 2013.
21. Zastempowski, B. Badanie Przepływu Oleju Przez Dławik Śrubowy. Ph.D. Thesis, Gdansk University of Technology, Gdansk, Poland, 1981.
22. Złoto, T. *Modelowanie Ociążenia Hydrostatycznego i Analiza Zjawisk Przepływowych w Szczelinie Rozrządu Tarczowego Pompy Wielotłoczkowej Osiowej*; Monografie/Politechnika Częstochowska; Wydawnictwa Politechn: Częstochowa, Poland, 2007; ISBN 978-83-7193-356-1.
23. Złoto, T.; Kowalski, K. Load of the Slipper-Swash Plate Kinematic Pair of an Axial Piston Pump. *MATEC Web Conf.* **2018**, *157*, 08013. [[CrossRef](#)]
24. Osiecki, A. *Hydrostatyczny Napęd Maszyn*; Wydawnictwa Naukowo-Techniczne: Warszawa, Poland, 1998; ISBN 978-83-204-2296-2.
25. Strmčnik, E.; Majdič, F. Comparison of Leakage Level in Water and Oil Hydraulics. *Adv. Mech. Eng.* **2017**, *9*, 168781401773772. [[CrossRef](#)]
26. Patrosz, P. Influence of Gaps' Geometry Change on Leakage Flow in Axial Piston Pumps. In *Advances in Hydraulic and Pneumatic Drives and Control 2020*; Stryczek, J., Warzyńska, U., Eds.; Lecture Notes in Mechanical Engineering; Springer International Publishing: Cham, Switzerland, 2021; pp. 76–89. ISBN 978-3-030-59508-1.
27. Edge, K.A.; Darling, J. Cylinder Pressure Transients in Oil Hydraulic Pumps with Sliding Plate Valves. *Proc. Inst. Mech. Eng. Part B Manag. Eng. Manuf.* **1986**, *200*, 45–54. [[CrossRef](#)]
28. Ye, S.-G.; Zhang, J.-H.; Xu, B. Noise Reduction of an Axial Piston Pump by Valve Plate Optimization. *Chin. J. Mech. Eng.* **2018**, *31*, 57. [[CrossRef](#)]
29. Bergada, J.M.; Kumar, S.; Davies, D.L.; Watton, J. A Complete Analysis of Axial Piston Pump Leakage and Output Flow Ripples. *Appl. Math. Model.* **2012**, *36*, 1731–1751. [[CrossRef](#)]
30. Javalagi, S.; Singireddy, S. *Hydraulic Fluid Properties and Its Influence on System Performance*; Linköpings Universitet: Linköpings, Sweden, 2012.
31. Rydberg, K.-E. Hydraulic Fluid Properties and Their Impact on Energy Efficiency. In Proceedings of the 13th Scandinavian International Conference on Fluid Power, Linköping, Sweden, 3–5 June 2013; Linköping University Electronic Press: Linköping, Sweden, 2013; pp. 447–453.
32. Knight, G.C. Water Hydraulics. *Tribol. Int.* **1977**, *10*, 105–108. [[CrossRef](#)]
33. Lim, G.H.; Chua, P.S.K.; He, Y.B. Modern Water Hydraulics—the New Energy-Transmission Technology in Fluid Power. *Appl. Energy* **2003**, *76*, 239–246. [[CrossRef](#)]
34. Patrosz, P.; Osiecki, L. CFD Analysis of a Flow in Commutation Window in PWK pump [Data Set]. Gdańsk University of Technology. 2021. Available online: <https://mostwiedzy.pl/pl/open-research-data/cfd-analysis-of-a-flow-in-commutation-window-in-pwk-pump,530084316516799-0> (accessed on 21 June 2021). [[CrossRef](#)]